Bertling, K., Perchoux, J., Taimre, T., Malkin, R., Robert, D., Rakić, A., & Bosch, T. (2014). Imaging of acoustic fields using optical feedback interferometry. *Optics Express*, *22*(24), 30346-30356. https://doi.org/10.1364/OE.22.030346

University of Bristol - Explore Bristol Research
General rights

Imaging of acoustic fields using optical feedback interferometry

Karl Bertling,[1] **Julien Perchoux,**[2,3,*] **Thomas Taimre,**[4] **Robert Malkin,**[5]
Daniel Robert,[5] **Aleksandar D. Rakić,**[1] **and Thierry Bosch**[2,3]

[1]*School of Information Technology and Electrical Engineering, The University of Queensland,
Brisbane, QLD 4072, Australia*
[2]*CNRS, LAAS, F-31400 Toulouse, France*
[3]*Univ de Toulouse, INP, LAAS, F-31400 Toulouse, France*
[4]*School of Mathematics and Physics, The University of Queensland, Brisbane, QLD 4072,
Australia*
[5]*School of Biological Sciences, University of Bristol, BS8 1TQ England, UK*

[*]*julien.perchoux@laas.fr*

Abstract: This study introduces optical feedback interferometry as a simple and effective technique for the two-dimensional visualisation of acoustic fields. We present imaging results for several pressure distributions including those for progressive waves, standing waves, as well as the diffraction and interference patterns of the acoustic waves. The proposed solution has the distinct advantage of extreme optical simplicity and robustness thus opening the way to a low cost acoustic field imaging system based on mass produced laser diodes.

© 2014 Optical Society of America

OCIS codes: (120.3180) Interferometry; (280.3420) Laser sensors; (140.2020) Diode lasers.

References and links

1. T. Fjield, X. Fan, and K. Hynynen, "A parametric study of the concentric-ring transducer design for MRI guided ultrasound surgery," J. Acoust. Soc. Am. **100**, 1220–1230 (1996).
2. O. Manneberg, J. Svennebring, H. M. Hertz, and M. Wiklund, "Wedge transducer design for two-dimensional ultrasonic manipulation in a microfluidic chip," J. Micromech. Microeng. **18**, 095025 (2008).
3. C. E. Ebbing and T. H. Hodgson, "Diagnostic tests for locating noise sources: Classical techniques and signal processing techniques," Noise Control Eng. **3**, 30–46 (1974).
4. K. Prestwich, "The energetics of acoustic signaling in anurans and insects," Amer. Zool. **34**, 625–643 (1994).
5. R. Wimberger-Friedl, "The assessment of orientation, stress and density distributions in injection-molded amorphous polymers by optical techniques," Prog. Polym. Sci. **20**, 369–401 (1995).
6. R. Malkin and D. Robert, "High sensitivity non-contact method for dynamic quantification of elastic waves and strains in transparent media," Measurement **55**, 51–57 (2014).
7. D. Ballantine Jr, R. M. White, S. J. Martin, A. J. Ricco, E. Zellers, G. Frye, and H. Wohltjen, *Acoustic Wave Sensors: Theory, Design, & Physico-Chemical Applications* (Academic, 1996).
8. A. J. Ricco, R. M. Crooks, and G. C. Osbourn, "Surface acoustic wave chemical sensor arrays: new chemically sensitive interfaces combined with novel cluster analysis to detect volatile organic compounds and mixtures," Acc. Chem. Res. **31**, 289–296 (1998).
9. E. G. Williams, J. Maynard, and E. Skudrzyk, "Sound source reconstructions using a microphone array," J. Acoust. Soc. Am. **68**, 340–344 (1980).
10. P. A. Chinnery, V. F. Humphrey, and C. Beckett, "The schlieren image of two-dimensional ultrasonic fields and cavity resonances," J. Acoust. Soc. Am. **101**, 250–256 (1997).
11. X. Jia, G. Quentin, and M. Lassoued, "Optical heterodyne detection of pulsed ultrasonic pressures," IEEE Trans. Sonics Ultrason. **40**, 67–69 (1993).
12. T. A. Pitts and J. F. Greenleaf, "Three-dimensional optical measurement of instantaneous pressure," J. Acoust. Soc. Am. **108**, 2873–2883 (2000).
13. N.-E. Molin,

Optical Methods for Acoustics and Vibration Measurements, in *Springer Handbook of Acoustics*, T. D. Rossing, ed (Springer, 2007).

14. L. Zipser, H. Franke, E. Olsson, N.-E. Molin, and M. Sjödahl, "Reconstructing two-dimensional acoustic object fields by use of digital phase conjugation of scanning laser vibrometry recordings," Appl. Opt. **42**, 5831–5838 (2003).

15. R. Malkin, T. Todd, and D. Robert, "A simple method for quantitative imaging of 2D acoustic fields using refracto-vibrometry," J. Sound Vib. **333**, 4473–4482 (2014).

16. A. Torras-Rosell, S. Barrera-Figueroa, and F. Jacobsen, "Sound field reconstruction using acousto-optic tomography," J. Acoust. Soc. Am. **131**, 3786–3793 (2012).

17. G. Giuliani, M. Norgia, S. Donati, and T. Bosch, "Laser diode self-mixing technique for sensing applications," J. Opt. A, Pure Appl. Opt. **4**, S283–S294 (2002).

18. R. Kliese, T. Taimre, A. Bakar, Y. L. Lim, K. Bertling, M. Nikolić, J. Perchoux, T. Bosch, and A. D. Rakić, "Solving self-mixing equations for arbitrary feedback levels: a concise algorithm," Appl. Opt. **53**, 3723–3736 (2014).

19. K. Otsuka, K. Abe, J.-Y. Ko, and T.-S. Lim, "Real-time nanometer-vibration measurement with a self-mixing microchip solid-state laser," Opt. Lett. **27**, 1339–1341 (2002).

20. M. Kössl and I. J. Russell, "Basilar membrane resonance in the cochlea of the mustached bat," Proc. Natl. Acad. Sci. USA **92**, 276–279 (1995).

21. E. Sadıkoğlu, E. Bilgiç, and B. Karaböce, "A laser pistonphone based on self-mixing interferometry for the absolute calibration of measurement microphones," Appl. Acoustics **65**, 833–840 (2004).

22. M. Fathi and S. Donati, "Simultaneous measurement of thickness and refractive index by a single-channel self-mixing interferometer," IET Optoelectron. **6**, 7–12 (2012).

23. L. Xu, S. Zhang, Y. Tan, and L. Sun, "Simultaneous measurement of refractive-index and thickness for optical materials by laser feedback interferometry," Rev. Sci. Instrum. **85**, 083111 (2014).

24. A. A. A. Bakar, Y. L. Lim, S. J. Wilson, M. Fuentes, K. Bertling, T. Taimre, T. Bosch, and A. D. Rakić, "On the feasibility of self-mixing interferometer sensing for detection of the surface electrocardiographic signal using a customized electro-optic phase modulator," Physiol. Meas. **34**, 281–289 (2013).

25. F. E. Jones, "Simplified equation for calculating the refractivity of air," Appl. Opt. **19**, 4129–4130 (1980).

26. P. E. Ciddor, "Refractive index of air: new equations for the visible and near infrared," Appl. Opt. **35**, 1566–1573 (1996).

27. T. Young, "The Bakerian lecture: Experiments and calculations relative to physical optics," Phil. Trans. R. Soc. Lond. **94**, 1–16 (1804).

28. L. E. Kinsler, A. R. Frey, A. B. Coppens, and J. V. Sanders, *Fundamentals of Acoustics* (John Wiley & Sons, 2000)

1. Introduction

Visualization of sound or pressure field propagation in gases, fluids, or transparent media is of major interest, with applications in a diverse range of topics, including acoustic transducer design [1, 2], noise source identification [3], insect hearing [4], effects of elastic waves and strain in solid materials [5, 6], and material and chemical identification [7, 8].

Reconstruction of the propagation of these acoustic fields can be realised using diverse techniques, such as with microphone arrays (which can interfere with the field being measured) [9], shadowgraphy (which can visualise a field but cannot quantify its pressure) [10], and optical measurement techniques [11–13] including laser Doppler vibrometry (LDV) [14–16]. Previous work has shown the potential of refracto-vibrometry for imaging of sound propagation in two dimensions (2D) [15]. However, the laser interferometer often required with LDV remains bulky and highly sensitive to mechanical perturbations.

One method which can mitigate the difficulties encountered when using LDV is optical feedback interferometry (OFI), which relies on the "self mixing" effect in lasers, and can be used in a number of different sensing modalities [17, 18]. Such OFI systems have previously been used to detect sound waves by monitoring the vibration of an exposed speaker or membrane [19–21]. A logical extension of previous work is to apply OFI sensing to directly measure the variation in the local pressure associated with the acoustic wave.

We propose here an ultra simplified OFI system designed to facilitate the direct sensing of the acoustic field, permitting its reconstruction as a 2D image. Thanks to the self-aligned

topology of OFI sensors, our measurement setup does not require any optical element besides a commercial laser diode, a collimating lens, and a light retroreflector.

2. Principles of operation

Sound is the propagation of a compression wave. The compression makes the air, or more generally the propagating medium, more dense thus inducing a change in the refractive index of the medium. This change can be measured in a number of different ways using interferometric techniques. The most common arrangement consists of a fixed light reflector forming an external cavity with the interferometer. The propagating acoustic wave then changes the index inside the external cavity, allowing detection by LDV [11, 14, 15]. This functionality of a conventional LDV interferometer can be effectively implemented in a simple OFI architecture, enabling one to measure variations in the refractive index of the medium in the external cavity. Previous work has demonstrated the potential of this approach through the measurement of the refractive index of thin films [22, 23] and measuring the effect of small changes in index in optical modulators placed inside the external cavity [24]. Therefore, applying the OFI technique to the 2D imaging of small changes in index caused by a propagating sound field opens a range of possibilities for pressure field visualisation.

A laser subject to optical feedback emits a power P_F that is calculated from the power emitted by the stand-alone laser P_0 as:

$$P_F = P_0 \left[1 + m\cos(\omega_F \tau)\right], \tag{1}$$

where m is a modulation index which is strongly dependent on the external optical cavity length and the external cavity reflectivity, ω_F is the laser frequency when it is subject to feedback, and τ is the external cavity round-trip time. In this application, the round-trip time can be expressed as the sum of two terms: $\tau = \tau_0 + \delta\tau$, where $\tau_0 = 2nL/c$ is a constant part (the round trip time in the external cavity of length L of ambient index n) and $\delta\tau$ is a variable part resulting from
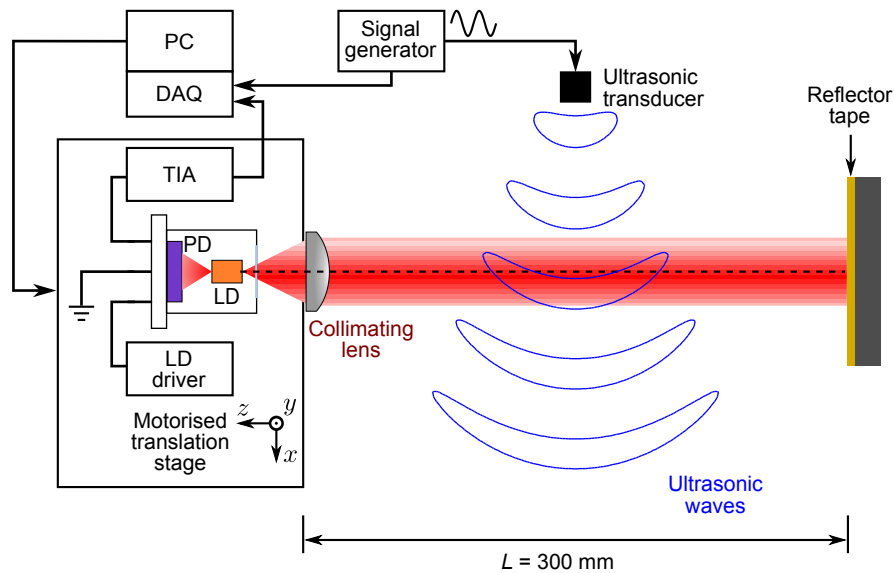

Fig. 1. Schematic diagram of the setup used for acoustic field measurements.

the compression of the propagation medium that induces a refractive index change of δn over the length L where the propagating acoustic wave overlaps with the laser beam:

$$\delta\tau = \int_0^L \frac{2\delta n(z)}{c}\, \mathrm{d}z. \tag{2}$$

The refractive index of air, in turn, depends on the local pressure in a linear fashion [25, 26]. The laser frequency itself varies with changes in external cavity optical length through the well-established phase condition [18].

The system will observe a line integral of the acoustic pressure field along the axis of the laser beam (z) varying with time t, resulting in an interferometric waveform at each spatial pixel. By varying the spatial position of the laser perpendicular to the beam axis (in an x–y plane as indicated in Fig. 1), a 2D array of interferometric signals captured. We may then observe these signals at a common time, say $t = 0$, to reduce the array to form a 2D image of the acoustic field integrated along the z axis at this particular moment.

3.   Experimental setup

Figure 1 shows the experimental setup. The laser diode (LD) used was a 785 nm Hitachi FP (HL7851) which was collimated with an aspheric lens (C-240, Thorlabs Inc.). A custom driver was used to operate the laser in continuous-wave mode at ≈ 80 mA (resulting in output power of ≈ 50 mW). The interferometric signal was monitored using the back facet photodiode (PD, mounted inside the laser package) with a custom built transimpedance amplifier (TIA). The laser, lens, and driver/receiver assembly was small enough to be mounted on an x–y motorised stage (LSM050A, Zaber Technologies Inc.), with the beam propagating perpendicular (along z) to the plane of travel of the stage. The fixed external target was a flat aluminium block covered with a retroreflector surface (Oralite Reflective Film 5700, ORAFOL Europe GmbH) and was placed at a distance 300 mm from the laser.

The source of sound was an ultrasonic piezoelectric transmitter (MA40B8S, Murata Manufacturing Co. Ltd.) which was driven from a signal generator (33210A, Agilent Technologies Inc.) with an ≈ 18 V sinusoidal waveform at a frequency of 40 kHz, producing an ≈ 108 dB SPL (sound pressure level, relative to 20 µPa) pressure wave at 40 kHz at a distance of 300 mm. The ultrasonic transmitter was placed midway ($z = 150$ mm) between the laser ($z = 0$ mm) and the retroreflective screen ($z = 300$ mm) and at a height of 110 mm above the surface of the optical table in order to produce an effectively sound wave propagating in free-space which travels perpendicular to the axis of propagation of the optical beam.

The signal from the PD is acquired over a 101 × 101 pixel scan area in a 40 × 40 mm area (0.4 mm step size , $x = 0$ to 40 mm $y = -20$ to +20 mm). The edge of the ultrasonic piezoelectric transmitter is situated just before $x = 0$ mm and centred at $y = 0$ mm. In order to reduce the effects of speckle from the retroreflective screen, each recorded waveform was comprised of an average of 10 signals which were measured with a 1 µm lateral step in between. Each of these signals was acquired with a sample rate of 1 MS/s using a 16-bit data acquisition card (NI-USB6251, National Instruments Co.) over four periods of the acoustic wave (100 µs trace). Typical signals from a single pixel, together with the stimulus signal, can be seen in Fig. 2. Each recorded four-period trace was triggered from the signal generator which was driving the ultrasonic transmitter. The periodicity in the measured signal results from the periodic driving signal. Hence, by triggering from the source driving the transmitter one acquires signals that, for all practical purposes, are acquired over the same relative acquisition window, the first time-point of which we designate $t = 0$.

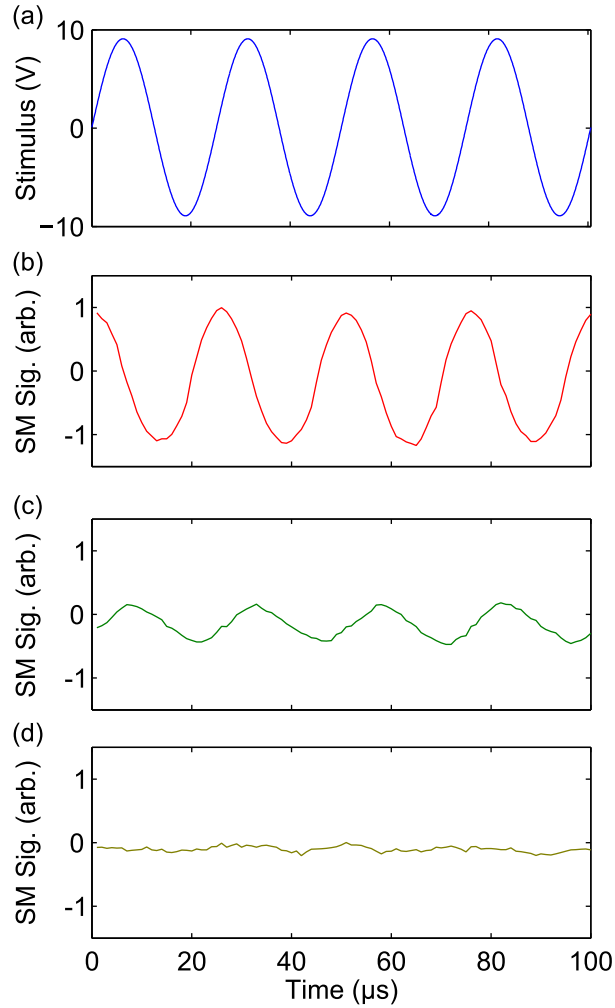Experimental results were compared with simulations which are described in the appendix.

Fig. 2. Typical signals from a single pixel. (a) Stimulus from signal generator. (b) Signal wave just next to the ultrasonic transmitter ($x = 0$ mm, $y = 0$ mm). (c) Signal wave at furthest point away from transmitter in the scan area in line with the axis of sound propagation ($x = 40$ mm, $y = 0$ mm). (d) Signal wave from area with minimal sound propagation ($x = 0$ mm, $y = 20$ mm). For further information about these three regions, see Fig. 3.

4. Results and discussion

Examining Fig. 2, we can see that each of the waveforms from each of the locations, show a distinct change depending on the measurement location. Amplitude and phase changes are readily apparent from the measurements made by the OFI sensor. This shows that minimal signal processing is required to extract amplitude and phase information directly, as well as for mapping the acoustic field.

The first acoustic field scanning experiment investigated an ultrasonic transmitter emitting to free space. The measured and simulated pressure fields agree almost perfectly (Fig. 3). Figure 3(a) shows the 2D scan with data for each pixel acquired from $t = 0$ s for each waveform (as seen in Fig. 2) in the 101 × 101 scan area. Media 1 shows the time evolution of this result as it steps t from 0–100 μs. Figures 3(b) and 3(c) show the amplitude and phase information for
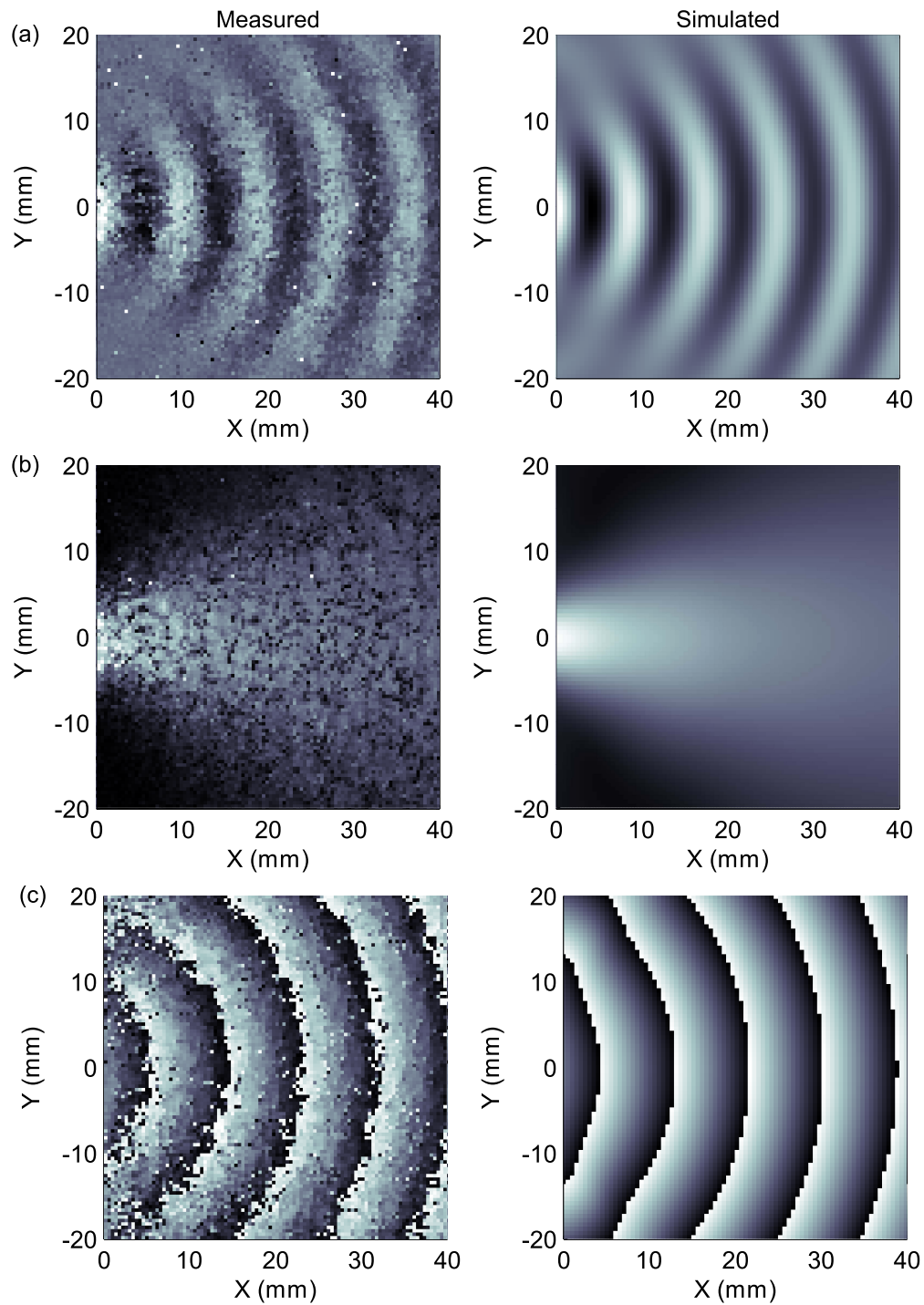
Fig. 3. Propagation of the acoustic field with the ultrasonic transmitter propagating the field into free space (see also Media 1); Left: Measured, Right: Simulation. (a) Image at $t = 0$ s. (b) Amplitude of acoustic field. (c) Phase of acoustic field.
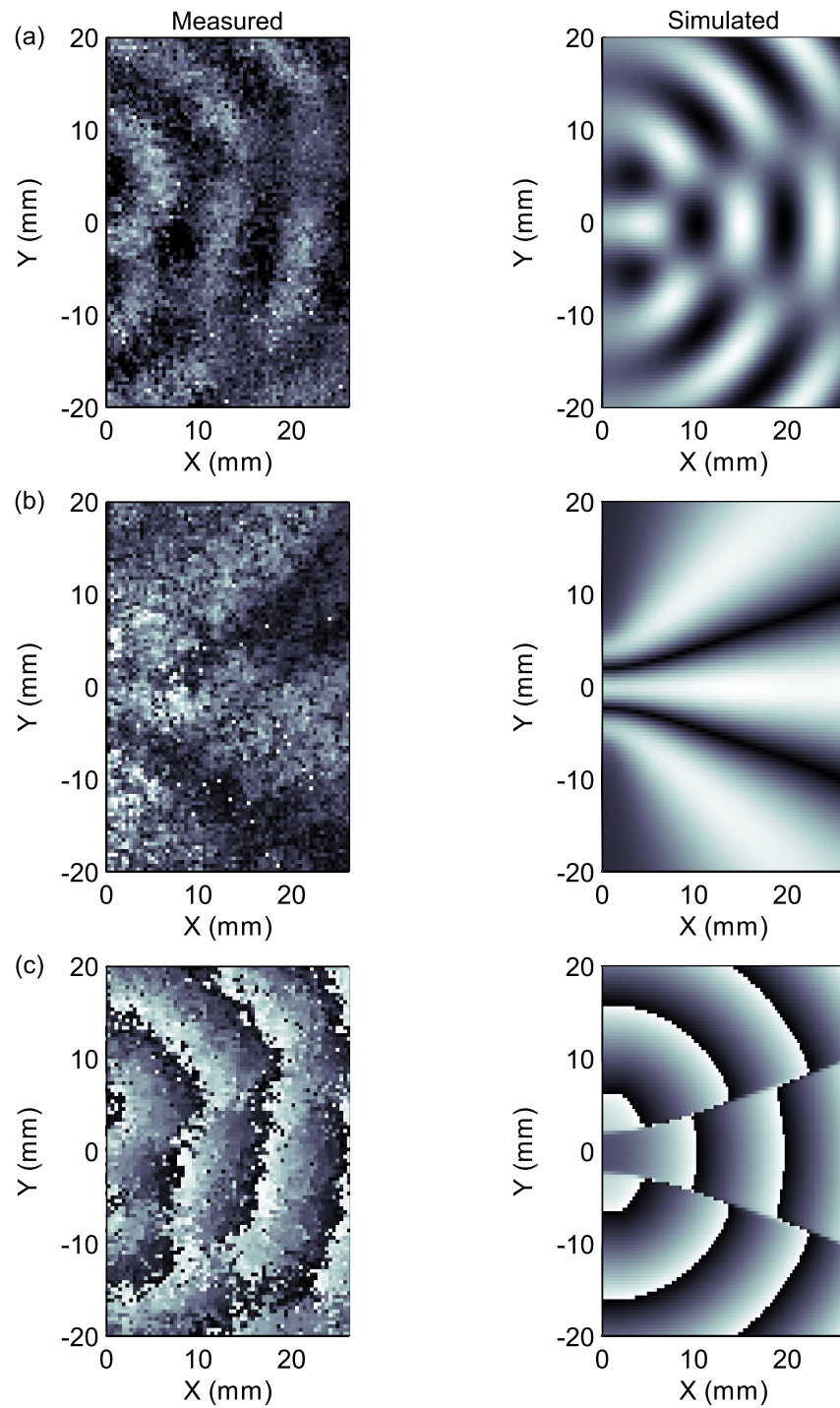
Fig. 4. Propagation of the acoustic field through two slits (see also Media 2); Left: Measured, Right: Simulation. (a) Image at $t = 0$ s. (b) Amplitude of acoustic field. (c) Phase of acoustic field.

each of these waveforms, calculated from the information in the fast Fourier transform (FFT) of each of the signals at 40 kHz.

Another interesting phenomenon to visualise is the patterns in the acoustic field, generated from multiple interfering waves. In order to observe this we propagated the emitted signal from the ultrasonic transmitter through two closely aligned slits, similar to Young's two slit experiment with light [27]. The slits were cut into a 200×200 mm^2 metal plate with the slits centred on the axis of propagation of the ultrasonic transmitter and are 2 mm wide, 100 mm long and spaced 10 mm apart. The ultrasonic transmitter was situated 20 mm from the metal plate. Figure 4 shows measured and simulated acoustic fields propagating from the slits. The displayed area has been clipped in order to emphasize the interference pattern (full field can be seen in Media 2). The slight discrepancy can be attributed to mechanical tolerances and misalignment of the experimental setup, the major expected features (as shown in the simulation) are still clearly visible.

Similarly we can also observe what happens when we have partial reflection from a corner obstruction blocking the acoustic field (Fig. 5). We can see the standing wave resulting from direct reflection in the amplitude plot [lower half of Fig. 5(b)] as well as diffraction pattern produced by the corner [upper half of Fig. 5(b), also observable in Media 3].

It is of practical interest to note that changes in the external cavity length appear to have limited effect on measured acoustic fields. In order to investigate this the flat retroreflector screen was replaced with a cylindrical glass beaker (diameter 91 mm) to which the retroreflective surface was affixed, thereby creating a curved screen for the measurement (that is, significantly varying the external cavity length). Figure 6(a) and 6(b) show the result from the flat retroreflector screen and from the curved retroreflective screen, respectively, and for all practical purposes both have identical behaviour. This was also observed even when the retroreflective surface was applied poorly — with noticeable bubbles or creases — to the screen. This means that the sensing system could still be viable when placed in a uncooperative environment where the retroreflective surface has to be attached to an uncooperative screen.

5. Conclusion

In summary we have demonstrated the use of OFI for the 2D imaging of an acoustic field. The system as demonstrated can cope with imaging propagation of sound waves as they interact with their environment. This method has the distinct advantage of simplicity, as it requires only a commercial laser diode, a collimating lens, and a light reflector, with minimal electronics and signal processing in order to realise the imaging of the acoustic field. This combined with the robustness when using a non-ideal retroreflector screen, opens the way to a low cost disposable acoustic field imaging system which could be deployed in harsh or destructive environments.

Appendix

Simulation of acoustic pressure field

The acoustic source used in this study (the disk-shaped piezoelectric transducer, with diameter of $R = 6.6$ mm) was modelled as a plane circular piston of radius R moving with time-harmonic velocity in the direction normal to the surface of the piston (transducer). To obtain the pressure at any field point we divided the surface of the transducer into infinitesimal elements, each of which was treated as a simple (point) source located on the surface of the transducer. Each of the point sources creates a spherical wave [28]. The complex form of the harmonic solution for the acoustic pressure of such a spherical wave at the field point (x,y,z) is
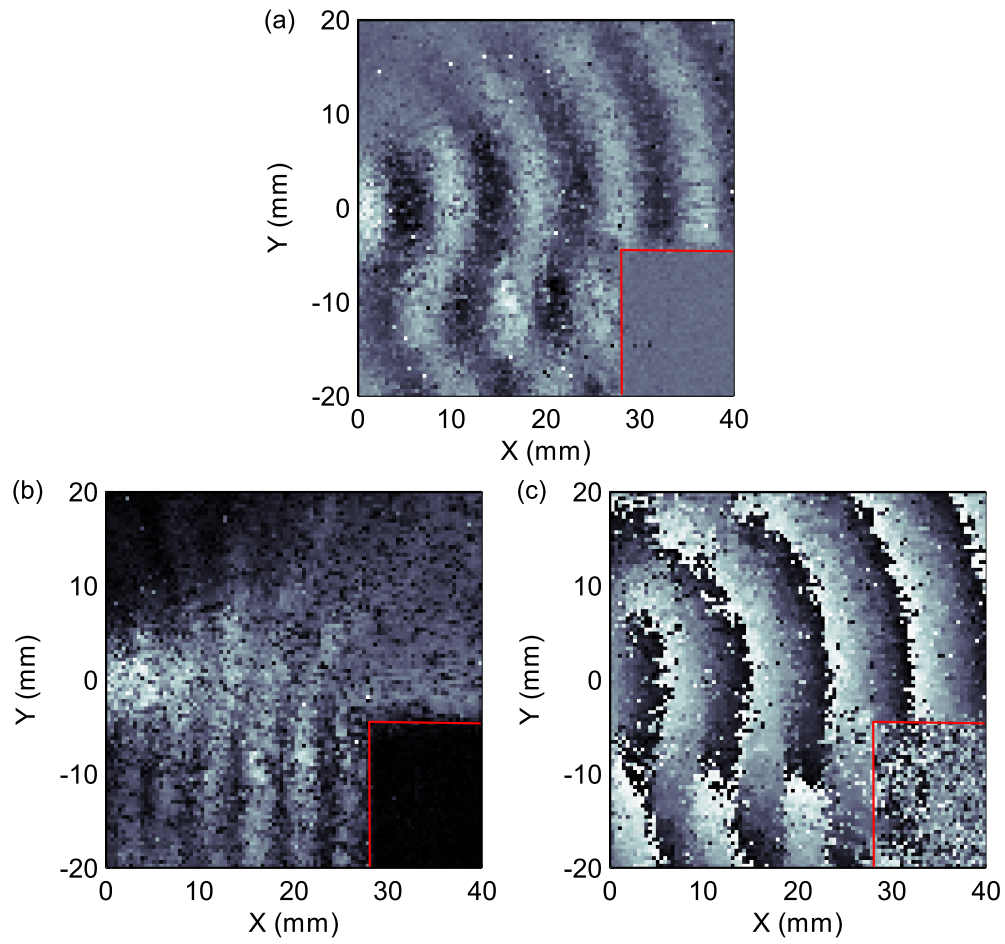
$$p(x,y,z,r',t) = A(r')e^{j(\omega t - kr')}, \tag{3}$$

Fig. 5. Measured signal with a reflector (aluminium block in lower right corner, indicated in red) partially blocking the sound field (see also Media 3); (a) Image at $t = 0$ s. (b) Amplitude of acoustic field. (c) Phase of acoustic field.
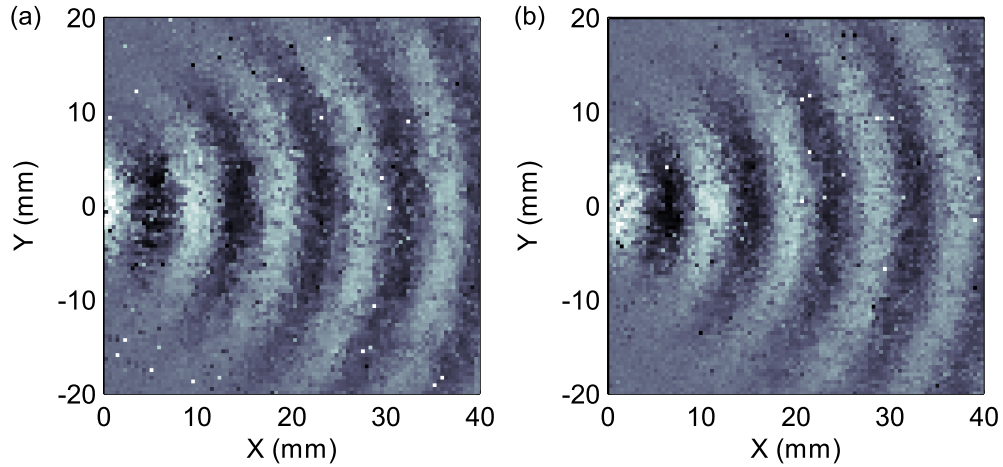
Fig. 6. Comparison between the acoustic fields from flat and curved retroreflector screens. (a) Flat retroreflector screen (external cavity constant). (b) Curved retroreflector screen (external cavity changing along the *x* axis).

where r' is the distance from the point source *i* located at (x_i',y_i',z_i') to the field point (x,y,z), ω is the angular frequency, *k* is the wavenumber, $\mathrm{j} = \sqrt{-1}$,

$$r' = [(x-x_i')^2 + (y-y_i')^2 + (z-z_i')^2]^{1/2},$$ (4)

and $A(r')$ can be approximated by $a/(1+br')$, (with constants *a* and *b* empirically set to $a = 1.8519$ and $b = 61.7284$).

Using the superposition principle, the total pressure generated at the field point is

$$P(x,y,z,r',t) \propto \int_S A(r')\mathrm{e}^{\mathrm{j}(\omega t - kr')}\mathrm{d}S,$$ (5)

where the surface integral is calculated over the entire surface of the transducer. The measured signal is proportional to the dynamic time delay $\delta\tau$ defined by (2), and in turn to the line integral of the dynamic pressure $p(x,y,z,r',t)$ along the *z* dimension, from the laser to the retroreflector and back. For simulation purposes, the speed of sound was taken as $c = 343$ m·s^{-1} and the frequency of the source as precisely $f = 40$ kHz, giving an associated angular frequency of $\omega = 2\pi f$ rad·s^{-1} and wavenumber $k = \omega/c$ rad·m^{-1}. Discrete approximation of the integral (5) has been calculated by considering the sources distributed over the emitting part of the ultrasonic transmitter — that is, the point sources lying on the disc and for the field-points in a three-dimensional grid over the space occupied by the ultrasonic wave. For *n* point sources on the disc, the resulting pressure *P* at field location (x,y,z) and time *t* is:

$$P(x,y,z,t) \propto \sum_{i=1}^{n} p(x,y,z,r_i',t).$$ (6)

Finally, the *z* dimension is marginalised by summing over all its entries (proportional to the standard discrete approximation of the line-integral), resulting in a quantity $\widetilde{P}$ proportional to the observed pressure:

$$\widetilde{P}(x,y,t) \propto \sum_z P(x,y,z,t).$$ (7)

Note that $\widetilde{P}(x,y,t)$ is a complex quantity. The amplitude of the simulated acoustic field is simply $|\widetilde{P}(x,y)| = \sqrt{\widetilde{P}(x,y)\,\widetilde{P}*(x,y)}$, where $*$ denotes complex conjugation, and the phase of the simulated acoustic field is $\arg(\widetilde{P}(x,y)) = \mathrm{atan}(\Im(\widetilde{P}(x,y))/\Re(\widetilde{P}(x,y)))$, where $\mathrm{atan}(y/x)$ is the four-quadrant arc-tangent.

The only change required for the two slit simulation was to "deactivate" any of the point sources which were located outside the slits of width 2 mm and length 100 mm with the slit centres separated by 10 mm and equally spaced around the centre of the simulated ultrasonic transmitter.

Acknowledgments